Oxygen vacancy dipoles in strained epitaxial $BaTiO_3$ films

M. Tyunina,[1,2,*] J. Peräntie,[1] T. Kocourek,[2] S. Saukko,[3] H. Jantunen,[1] M. Jelinek,[2] and A. Dejneka[2]

[1]*Microelectronics Research Unit, Faculty of Information Technology and Electrical Engineering, University of Oulu, P. O. Box 4500, FI-90014 Oulu, Finland*

[2]*Institute of Physics of the Czech Academy of Sciences, Na Slovance 2, 18221 Prague, Czech Republic*

[3]*Center of Microscopy and Nanotechnology, University of Oulu, P. O. Box 8000, FI-90014 Oulu, Finland*

(Received 28 November 2019; revised manuscript received 26 January 2020; accepted 18 March 2020; published 20 April 2020)

The existence of out-of-plane-oriented oxygen vacancy dipoles was experimentally established in (001) perovskite epitaxial films of ferroelectric barium titanate by analyses of the crystal and electronic structure as well as the ferroelectric and optical properties. The formation of the defects was shown to occur in the presence of in-plane compressive strain and oxygen-deficient deposition conditions. The in-plane compressive strain was suggested to favor the formation of oxygen vacancies V_O in the Ba-O planes and thus stabilize the out-of-plane orientation of the dipolar $(V^{+2}{}_O\text{-}Ti^{3+})^+$ defects.

DOI: 10.1103/PhysRevResearch.2.023056

I. INTRODUCTION

Barium titanate ($BaTiO_3$, BTO) is one of the best-studied perovskite oxide ferroelectrics, which are known for their large switchable spontaneous polarization and excellent piezoelectric, pyroelectric, photovoltaic, electrocaloric, and other properties, as well as devices based thereon [1–4]. The polarization and charge-transport properties, important for applications, depend on the presence of unintentional or intentional point defects in ferroelectrics. It is worth mentioning that oxygen vacancies are the most common point defects in perovskite oxides. In titanate ferroelectrics such as BTO and $SrTiO_3$ (STO), oxygen vacancies V_O may exist as neutral ($V^0{}_O$), singly positive ($V^+{}_O$), and/or doubly positive ($V^{+2}{}_O$) ones [5–10]. The vacancy $V^{+2}{}_O$ can trap one to two electrons in the form of small polarons. In such polarons, the electrons are localized on Ti atoms near the vacancy, which changes Ti^{4+} to Ti^{3+} [5,6]. The lowest formation energy is found for the doubly charged vacancies $V^{+2}{}_O$ and the complexes of $V^{+2}{}_O$ and one polaron, or $(V^{+2}{}_O\text{-}Ti^{3+})^+$ [5,6].

In practice, the oxygen vacancies form to compensate the charge imbalance induced by heterovalent doping and/or in the result of oxygen-deficient processing such as synthesis or annealing in a reducing atmosphere [11–13], or during thin-film deposition at sufficiently low oxygen pressures [14–16]. In epitaxial films, the influence of lattice strain on the formation of oxygen vacancies was also recently recognized [17–20].

Here we demonstrate the formation of oxygen vacancy dipoles occurring under a combined action of low-pressure deposition and in-plane compressive strain in epitaxial BTO films. By analyzing the crystal and electronic structures, ferroelectric behavior, and optical properties of the films, we establish the presence and out-of-plane orientation of $(V^{+2}{}_O\text{-}Ti^{3+})^+$ defects. We discuss the strain-driven formation of these defects.

II. EXPERIMENT

Thin films of BTO (∼150 nm) were deposited with $SrRuO_3$ (∼15–20 nm, SRO) bottom electrode layers and also without such layers on epitaxially polished single-crystal (001) $SrTiO_3$ (STO) substrates (MTI Corp.). The BTO and SRO films were grown by pulsed laser deposition (PLD) using a KrF excimer laser (wavelength 248 nm, energy density ∼2 J/cm^2, pulse repetition rate 2 Hz) at a substrate temperature of 973 K. The ambient oxygen pressure during SRO deposition was 20 Pa. The BTO films were deposited using different pressures of 0.1, 2, 5, 10, and 20 Pa. In addition to the 150-nm-thick BTO films, BTO films of different thicknesses (∼35 and ∼70 nm) were deposited at a pressure of 5 Pa. Postdeposition cooling was conducted at a rate of 5 K/min and the BTO deposition pressure. Capacitor stacks were formed using a bottom SRO electrode layer and circular top Pt contact pads (area 0.2 mm^2), which were created by a room-temperature vacuum PLD of Pt through a shadow mask.

The crystal structure of the films was studied by high-resolution x-ray diffraction (XRD) with a D8 DISCOVER diffractometer (Bruker corporation) using Cu Kα radiation. Θ-2Θ scans in the range of $2\Theta = (10-130)$ deg and reciprocal space maps (RSM) in the vicinity of the perovskite (002) and (103) diffractions were acquired. The in-plane (parallel to substrate surface) and out-of-plane (normal to substrate surface) lattice parameters were estimated from the positions of the diffraction maxima using STO as a reference.

*Corresponding author: marina.tjunina@oulu.fi

The local crystal structure was inspected by transmission electron microscopy (TEM) and high-resolution transmission electron microscopy (HRTEM) using a JEOL JEM-2200FS microscope operated at 200 kV. Cross-sectional samples were prepared for analysis by focused ion beam (FIB) milling using a Dual-Beam scanning electron microscope FEI Helios Nanolab 600 equipped with a Ga+ FIB. The bright-field TEM (BF-TEM), scanning TEM (STEM), selected area electron diffraction (SAED), nanobeam electron diffraction (nBED), and HRTEM imaging combined with fast Fourier transforms (FFT) and Fourier filtering were employed to investigate the crystal structure of BTO. Energy dispersive x-ray spectroscopy (EDS) and electron energy loss spectroscopy (EELS) were utilized to define the elemental composition. The EDS and EELS spectra were acquired and quantified using GATAN software.

A special algorithm was applied to accurately quantify the spatial distribution of the lattice parameters in the in-plane and out-of-plane directions inside the BTO film deposited at 5 Pa. The algorithm was as follows. The HRTEM images with a field of view ∼(50 nm×50 nm) were acquired along the out-of-plane [100] axis and in-plane [001] axis of BTO. The images overlapped and covered the whole BTO film in the out-of-plane direction and a region with a width of ∼150 nm in the in-plane direction. The (010) and (001) interplanar distances, corresponding to the in-plane and out-of-plane lattice parameters of BTO, were extracted from fast Fourier transforms of the images using a sliding-window technique and CRYSTBOX DIFFRACT GUI software [21,22]. The lattice parameters were estimated as a function of the position in the film using averaging and binning of the data extracted from each of the windows. Compared to the widely applied geometrical phase analysis (GPA), this approach ensures better accuracy in our films [21,22]. The lattice parameters were determined with an accuracy of ±0.005 Å.

The impedance of the capacitors was measured by a NOVOCONTROL Alpha-AN High Performance Frequency Analyzer. The ferroelectric polarization was inspected by using a TF 2000E Analyzer (aixACCT Systems GmbH). In all measurements, the electric field was applied and the response was measured along the out-of-plane direction for the SRO/BTO/Pt capacitors.

The local piezoresponse was investigated by piezoresponse force microscopy (PFM) using Multimode 8 atomic force microscope (Bruker) and Pt-coated silicon tips (HQ:NSC18/Pt, MikroMasch). The out-of-plane PFM signal was acquired at a probing ac voltage of 2 V and as a function of superposed dc voltage, which was swept in the range of −8 to 8 V.

The optical constants (index of refraction, extinction coefficient, and absorption coefficient) of the BTO films were studied using variable angle spectroscopic ellipsometry. The measurements were carried out on a J. A. Woollam ellipsometer (wavelengths of 146–1600 nm) at room temperature in an atmosphere of dry nitrogen. The ellipsometric spectra were taken at incident angles of 65 and 70 deg. The dielectric functions and optical constants of the films were extracted from the ellipsometric spectra using a commercial WVASE32 software package. More details for the ellipsometric procedures can be found elsewhere [23–25].

III. RESULTS

A. Crystal structure

XRD and TEM studies evidenced a cube-on-cube-type epitaxy for all the BTO and SRO films on STO. The BTO films are perovskite-type and oriented with the (00l) planes parallel to the (001) plane of STO (Fig. S1 in Supplemental Material [26]). Other phases were not detected. Inspections of the elemental composition by EDS and EELS did not reveal stoichiometric deviations either. The SRO layers grow pseudomorphically on STO (Supplemental Material in Figs. S2 and S3 [26]): the in-plane lattice parameters of the perovskite SRO cell are equal to those of the underlying STO.

For the 150-nm-thick BTO films, the measured out-of-plane and in-plane lattice parameters (c and a), tetragonality ($c/a - 1$), and unit-cell volume $V_{uc} = a^2c$ are summarized in Fig. 1. The shadowing in Fig. 1(c) qualitatively illustrates an out-of-plane spread of the parameter c as extracted from the full width at half maximum of the (003) Θ-2Θ diffraction peaks (Supplemental Material in Fig. S1).

The results in Fig. 1 reveal that the BTO lattices apparently differ for different pressures.

The high-pressure 20-Pa film possesses an in-plane elongation and out-of-plane shrinkage compared to bulk BTO: $a > a_{BTO}$ and $c < c_{BTO}$, where $a_{BTO} = 3.992$ Å and $c_{BTO} = 4.036$ Å are the BTO bulk parameters. This behavior implies that the substrate-imposed in-plane compressive misfit strain s_a is relaxed ($s_a = a_{STO}/a_{0BTO} - 1 \approx -2.5\%$, where a_{STO} is the lattice parameter of STO and a_{0BTO} is the lattice parameter of a cubic cell of BTO $a_{0BTO} = {V_{uc}}^{1/3}$). Because of a mismatch between the thermal expansion coefficients of BTO and STO, a thermal biaxial in-plane tensile strain builds-up during postdeposition cooling [27]. Assuming a complete misfit relaxation during BTO growth at 973 K, the estimated room-temperature thermal strain is $s_T \approx 0.3\%$. The lattice parameters, tetragonality, and unit-cell volume of thermally strained BTO/STO were calculated using the elastic constants of BTO [28]. The measured negative tetragonality agrees well with the calculated value of −0.8%. The measured unit-cell volume is also consistent with the calculated volume of ∼64.4 Å^3. The proper unit-cell volume indicates the absence or a minor density of point defects in the high-pressure film. The film adopts the theoretically predicted a-phase [29,30]. Thus, the complete relaxation of misfit strain and the proper oxygen content are characteristics of our high-pressure BTO films.

With decreasing pressure, the unit-cell volume increases [Fig. 1(d)]. This lattice expansion is compatible with the previous observations in epitaxial films and commonly ascribed to the formation of oxygen vacancies therein [15,16,31–35]. However, compared to bulk stoichiometric BTO, the expansion reaches 2–3%, which exceeds that achieved for maximum allowed oxygen deficiency or for oxygen substitution in perovskite phase of BTO [36,37]. Assuming, nevertheless, that the expansion is macroscopically isotropic chemical one, the estimated misfit strain is up to $s_a \approx -3.3\%$ in the oxygen-deficient films. Such a large strain should have been completely relaxed in the 150-nm-thick films. In contrast to this expectation, the 0.1–5-Pa films exhibit profound out-of-plane elongation [Fig. 1(a)] and enhanced tetragonality [Fig. 1(c)].

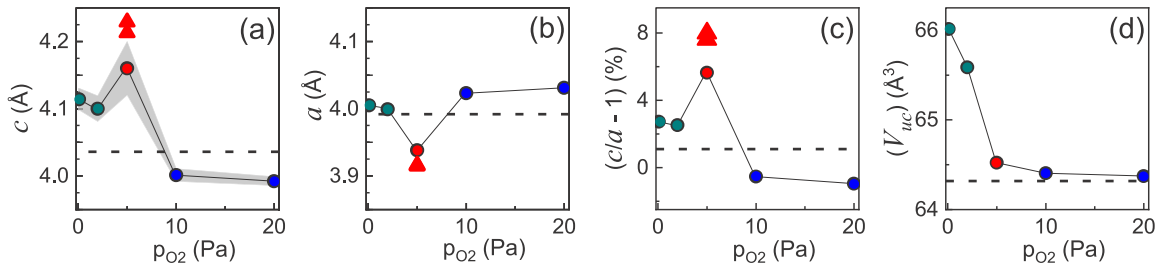

FIG. 1. (a) Out-of-plane and (b) in-plane lattice parameters, (c) tetragonality, and (d) unit-cell volume as a function of oxygen pressure during the deposition of 150-nm-thick BTO films. Data for the 5-Pa thinner films are also shown (red triangles). Dashed lines show reference values for bulk BTO.

Moreover, the 5-Pa films are nearly pseudomorphic to STO [Fig. 1(b)]. These observations imply that ordinary chemical expansion is insufficient for understanding the structural changes in the BTO films.

To elucidate possible role of strain, the peculiar films deposited at 5 Pa are analyzed in more details. The films are practically pseudomorphic to STO ($a \approx a_{STO} < a_{BTO}$) and demonstrate a strong out-of-plane elongation ($c \gg c_{BTO}$) with tetragonality up to ~8%. The lattice parameters, tetragonality, and unit-cell volume of pseudomorphic stoichiometric BTO were calculated assuming that the BTO/STO misfit strain does not relax and overrides the thermal mismatch. The measured tetragonality of ~8% and unit-cell volume of ~64.6 Å^3 exceed the calculated ones of ~5.8% and ~63 Å^3, respectively. This discrepancy is in line with the oxygen-vacancy-induced expansion of unstressed film's material and, hence, somewhat larger misfit strain in the oxygen-deficient films compared to that in the stoichiometric films assumed in the calculations. Thus, the pseudomorphic growth and anisotropic lattice expansion of the 5-Pa films suggest that the common relaxation of the substrate-imposed misfit strain can be hindered by the formation of oxygen vacancies.

With reducing pressure below 5 Pa, the misfit strain is further enlarged that leads to its partial relaxation. The structural changes as a function of pressure (Fig. 1) emerge from the combined action of misfit strain and oxygen deficiency. When taken separately, neither strain, nor oxygen vacancies can explain these changes.

To unfold strain-vacancy links, the films' microstructure is scrutinized. The cross-sectional TEM analysis unveils a column-free microstructure in the super-tetragonal 5-Pa BTO film, in contrast to the presence of columns in the other films [Figs. 2(a) to 2(c)]. The columns imply the Stranski-Krastanov growth mode, caused mainly by the relaxation of misfit strain through the formation of dislocations [38]. The absence of columns points to an additional phenomenon, other than the formation of dislocations in the 5-Pa film [Fig. 2(b)]. The local HRTEM analysis shows a change in the lattice parameters across the thickness, but not along the plane at each thickness [Figs. 2(d) to 2(f)]. The out-of-plane lattice parameter decreases from ~4.19 Å at the bottom to ~4.10 Å at the top [Fig. 2(d)]. The changes agree with the XRD observations in the 5-Pa films of different thicknesses (Supplemental Material in Fig. S1). The bottom-to-top lattice transformation takes place without a massive generation of dislocations and columns. The formation of low-angle boundaries is detected only at a distance of ~80 nm from the SRO/BTO interface (Supplemental Material in Fig. S4). Such a pseudomorphic growth can be ensured by the presence of point-type defects, which reduce the in-plane compression. The defects are generated under oxygen deficiency and are oxygen vacancies.

B. Ferroelectric behavior

The high-pressure 10–20-Pa films retain the ferroelectric *a*-phase with the in-plane spontaneous polarization, which is manifested by slim out-of-plane polarization-voltage loops (Supplemental Material in Fig. S5). The 2-Pa and 5-Pa films are ferroelectric with out-of-plane switchable polarization (Fig. 3 and Supplemental Material in Fig. S5). The large leakage current prevents polarization measurement in the 0.1-Pa films.

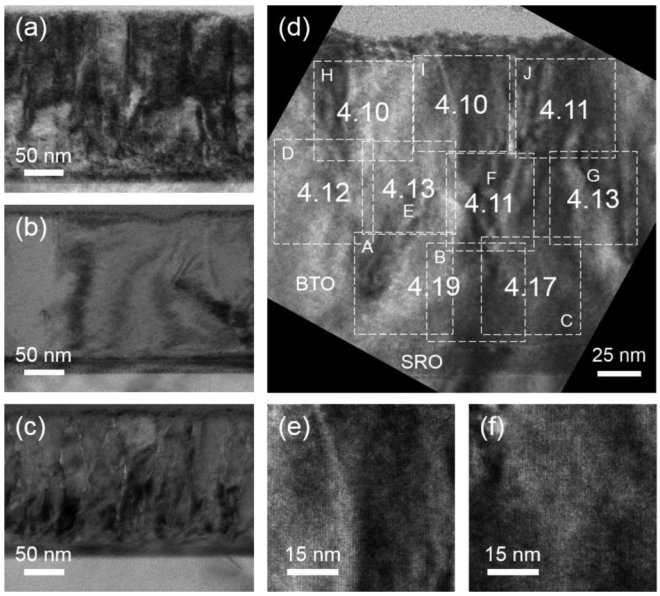

FIG. 2. Cross-sectional TEM analysis of the BTO films on SRO/STO. (a)–(c) Bright-field TEM images of the BTO films deposited at (a) 0.1, (b) 5, and (c) 20 Pa. (d) HRTEM image of the 5-Pa BTO film. Dashed lines and symbols (A)–(J) mark the analyzed regions. The determined out-of-plane lattice parameters are also shown therein. (e), (f) Representative HRTEM images from regions (e) I and (f) C at the top and bottom of the 5-Pa BTO film in (d).

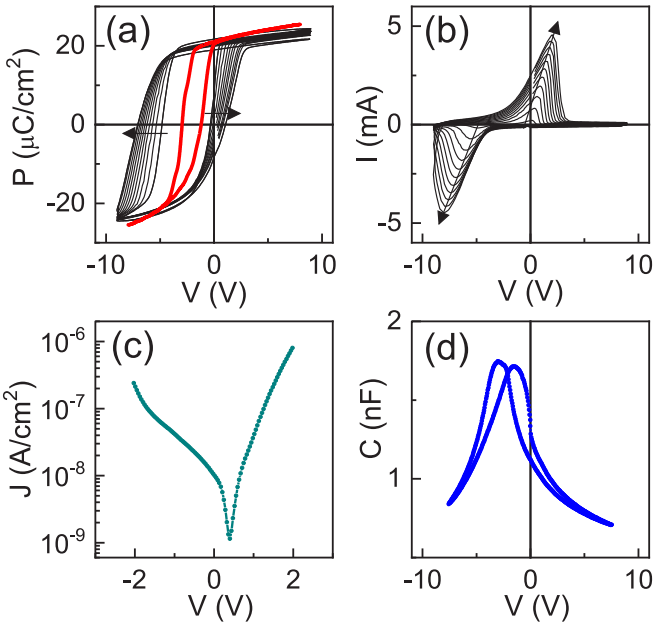

FIG. 3. (a) Polarization–voltage and (b) current–voltage loops, (c) density of leakage current, and (d) capacitance–voltage loop in the 5-Pa BTO film. Arrows in (a), (b) show the directions of frequency increase from 100 Hz to 5 kHz for the dynamic loops. Thick curve shows the quasistatic polarization in (a).

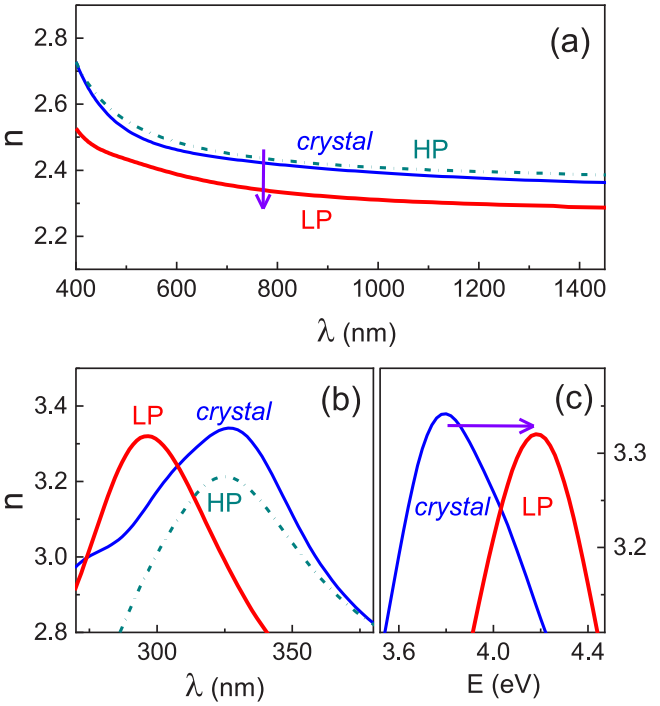

FIG. 4. Refraction coefficient as a function of (a), (b) wavelength and (c) photon energy in the 5-Pa BTO film (thick solid curves marked by LP), polydomain crystal (solid curves marked by *crystal*), and 20-Pa film (dashed curves marked by HP). Arrows indicate a change of (a) refraction and (c) a blueshift of the main peak in the 5-Pa film compared to the crystal.

The 5-Pa films exhibit the nearly rectangular well-saturated polarization-voltage (*P*-*V*) loops [Fig. 3(a)] and current-voltage loops [Fig. 3(b)]. The magnitude of the positive and negative saturation polarization is $\sim 25\,\mu\mathrm{C/cm^2}$ and close to the handbook room-temperature spontaneous polarization in bulk unstressed BTO [28]. This polarization similarity shows that neither lattice strain nor strain gradient are responsible for the ferroelectric properties here. Importantly, the ferroelectric loops are shifted along the voltage axis. The coercive voltages are of the same sign (negative here): the film possess an in-built electric field and is self-polarized. With increasing frequency, the coercivity increases, but the saturation polarization does not change [Figs. 3(a) and 3(b)]. This dynamic behavior (under an applied ac electric field) is consistent with the creep and flow motions of back-switched domains in high-quality epitaxial ferroelectric films [39]. The small density leakage current also complies with that found in high-quality epitaxial ferroelectric films [Fig. 3(c)]. The butterfly type capacitance-voltage loop confirms the ferroelectric switching and voltage offset in the 5-Pa BTO film [Fig. 3(d)].

The presence of the in-built field and self-polarization in the 5-Pa film without top Pt electrodes is confirmed by piezoresponce force microscopy (Supplemental Material in Fig. S6). The phase of the piezoresponse is around -90° over the film surface at zero bias. The phase changes by $\sim 180^\circ$ upon biasing and exhibits both the hysteresis and voltage offset, in agreement with the polarization switching measured using the top Pt electrodes.

The ferroelectric properties of the supertetragonal 5-Pa BTO films are akin to those of high-quality epitaxial perovskite ferroelectric films. Peculiarly, these films possess the in-built electric field and self-polarization. The in-built field is also present in the 2-Pa films (Supplemental Material in Fig. S5).

C. Optical properties

To discard the possible influence of electrodes and strain-induced single-domain state on the in-built field and self-polarization, we investigate spectra of optical constants in the films without electrodes. In particular, we compare the index of refraction n measured in the transparency range (at wavelengths $\lambda > 400$ nm) in the 5-Pa film and the reference polydomain BTO crystal [Fig. 4(a)]. The smaller n in the film arises due to fundamental electro- and elasto-optic effects in BTO [40,41]. Considering the out-of-plane in-built field E_{out} and strain s_{out} (due to lattice elongation) in the film, the drop in refraction can be presented as $[\Delta(n^{-2}) = r_{\mathrm{BTO}}E_{\mathrm{out}} + p_{\mathrm{BTO}}s_{\mathrm{out}}]$, where r_{BTO} and p_{BTO} are the electro- and elasto-optic coefficients of BTO, respectively. Using the maximum coefficients [41] $r_{\mathrm{BTO}} \approx 1300\,\mathrm{pm/V}$ and $p_{\mathrm{BTO}} \approx 0.05$ and strain $s_{\mathrm{out}} \approx 0.03$, we estimated a minimum field E_{out} from the refraction data. The optically estimated field is $E_{\mathrm{out}} \approx 8\,\mathrm{MV/m}$, which discards the electrodes and strain as its possible origin.

The in-built field is corroborated by the higher energies of the main optical transitions in the 5-Pa films compared to the reference crystal (as found here from the positions of the peaks in the refraction spectra) [Figs. 4(b) and 4(c)]. The peak in the film is blueshifted to shorter wavelengths (higher photon energies). The blueshift evidences an uplift

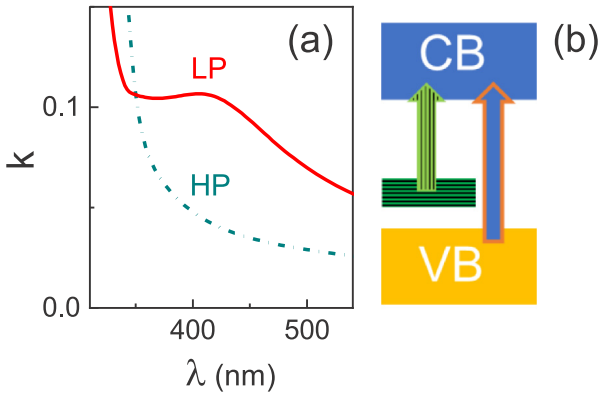

FIG. 5. Extinction coefficient as a function of wavelength in the 5-Pa (thick solid curve marked by LP) and 20-Pa (dashed curve marked by HP) BTO films. (b) Schematics for the optical excitations in the LP films.

of the conduction bands [40,42], which contrasts with a common spectral redshift (band-gap narrowing) under lattice expansion [43,44]. Therefore, the observed blueshift proves the presence of in-built field in the electrodeless 5-Pa film. Moreover, using polarization potentials, the blueshift ΔE can be expressed as $\Delta E = \beta P^2$, were P is the polarization and β is the temperature-independent band-edge polarization potential [45]. The detected blueshift $\Delta E \approx 0.4\,\text{eV}$ [Fig. 4(c)] corresponds to the polarization of $\sim 50\,\mu\text{C/cm}^2$, which is estimated using $\beta = 1.16\,\text{eV} \cdot \text{m}^4 \cdot \text{C}^{-2}$ of bulk BTO crystal. Because the value of β in the oxygen-deficient supertetragonal BTO film is not exactly known, the estimation is not accurate. Nevertheless, it supports the presence of significant self-polarization in the 5-Pa film without electrodes.

We emphasize that the index of refraction from the transparency range and the position of the main refraction peak in the 20-Pa films are similar with those in the reference crystal [Fig. 4]. These optical observations agree with the electrical data and confirm that the in-built field and self-polarization are the properties of the 5-Pa films.

Because optical transitions from/to defect-related in-gap states are the fingerprints of the defects, the presence of point defects can be detected optically. To reveal the in-gap states, we examine the defect-containing 5-Pa film and the reference defect-free 20-Pa film. Compared to the near-gap spectrum of the extinction coefficient k in the 20-Pa film [dashed curve in Fig. 5(a)], an additional hump at approximately 410 nm is observed in the 5-Pa film [solid curve in Fig. 5(a)]. This additional absorption is consistent with the optical excitation (at wavelengths shorter than 500 nm) of the $(V^{+2}_O\text{-}Ti^{3+})^+$ defects [46]. The corresponding in-gap states are schematically shown in Fig. 5(b).

In addition to the pre-edge absorption due to the in-gap states, the absorption edge is blueshifted to shorter wavelengths (higher photon energies), which evidences a band-gap widening in the 5-Pa film [Fig. 5(a)]. This near-edge behavior fully agrees with the blueshift in the refraction spectra and substantiates the presence of in-built field. While the pre-edge optical absorption is consistent with the excitation of $(V^{+2}_O\text{-}Ti^{3+})^+$ complexes, the in-built field

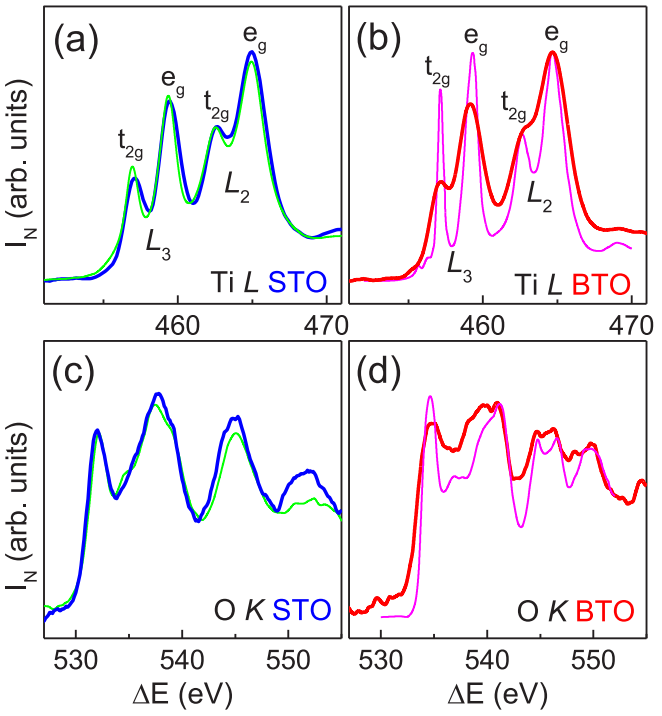

FIG. 6. Normalized EELS spectra at the (a), (b) Ti L-edge and (c), (d) O K-edge in the (a), (c) STO substrate and (b), (d) 5-Pa BTO film. Thin curves show the reference spectra for the (a), (c) STO and (b, d) BTO crystals.

can result from an out-of-plane dipolar ordering of these defect complexes.

D. Electronic structure

The presence of $(V^{+2}_O\text{-}Ti^{3+})^+$ complexes is further validated by detecting the Ti valence state from EELS Ti L-edge and O K-edge spectra in the 5-Pa BTO film [Fig. 6]. The reference spectra acquired from the STO substrate [Figs. 6(a) and 6(c)] agree with the published data [47,48] and attest to the correct measurements.

The Ti L-edge spectrum measured in the BTO film [Fig. 6(b)] is compared to that reported for a stoichiometric unstressed BTO crystal [49]. The film is characterized by a relative increase in the spectral weight of the Ti $L_{2,3}$ e_g peaks, especially in the lower-energy L_3-edge. Previously, such spectral changes were observed with increasing Ti^{3+} content in the nominally Ti^{4+}-based perovskite oxides [50,51]. The behavior of the Ti L-edge in the BTO film implies the presence of Ti^{3+} cations therein. Additionally, the valleys between the peaks at the O K-edge are lifted up in the film compared to the reference crystal [Fig. 6(c)]. This behavior also substantiates the presence of Ti^{3+} states in the BTO film [51].

We note that compared to the nominal $[Ti^{4+}O_6]$ octahedron in BTO, the $[Ti^{3+}O_5V_O]$ unit containing oxygen vacancy was shown to be elongated along the V_O-Ti axis [52,53]. Here the observed anomalous out-of-plane lattice elongation supports the presence of the out-of-plane oriented $(V^{+2}_O\text{-}Ti^{3+})^+$ defects in the 5-Pa BTO films.

IV. DISCUSSION

Thus, the strong out-of-plane elongation, in-built electric field, optical properties, and local electronic structure are all consistent with the presence of the out-of-plane oriented dipolar $(V^{+2}{}_O\text{-}Ti^{3+})^+$ defects in the oxygen-deficient BTO films. The defects emerge at low oxygen pressures and large biaxial in-plane compressive strain. We emphasize that neither supertetragonal structure, nor in-built field are obtained in the absence of such strain (Supplemental Material in Fig. S7).

The links between strain and oxygen vacancies are highlighted by recent first-principles analyses [18–20]. Compared to unstressed perovskite oxide ferroelectric, an in-plane compressive strain strongly reduces the formation energy for an out-of-plane oxygen vacancy [20]. That is, in the BTO films on STO, the in-plane compression facilitates the formation of oxygen vacancies in the Ba-O planes parallel to the substrate surface (Supplemental Material in Fig. S8) [54]. Moreover, the compressive strain is likely to intensify the formation of the $V^{+2}{}_O$ vacancies compared to the $V^0{}_O$ vacancies [20]. Considering that the out-of-plane $V^{+2}{}_O$ oxygen vacancies (i.e., $V^{+2}{}_O$ vacancies in the Ba-O planes) are favored by the in-plane compression and that the formation energy is low for the $(V^{+2}{}_O\text{-}Ti^{3+})^+$ defects in BTO [5,6], the formation of the out-of-plane oriented $(V^{+2}{}_O\text{-}Ti^{3+})^+$ complexes is preferred in the compressively strained oxygen-deficient BTO films.

The anisotropic formation of the oxygen vacancies (in the Ba-O planes) can boost anisotropic lattice expansion and enhance the out-of-plane elongation of the unit cell. Concurrently, our observations indicate that the formation of oxygen vacancies can partially release the substrate-induced misfit, in resemblance with the theoretical scenario [18].

In addition to the strain-controlled formation of oxygen vacancies also the migration of oxygen vacancies is governed by strain. For instance, for the compression-promoted out-of-plane vacancies, migration of vacancies in the out-of-plane direction is impeded [20]. (This restriction can be qualitatively understood from Supplemental Material in Fig. S8.)

The oxygen vacancy dipoles can efficiently tune the ferroelectric and optical behavior of BTO. These defects may influence the charge transport and, possibly, exhibit magnetism leading to multiferroic states. Comprehensive theoretical investigations of the formation and structure of oxygen-vacancy-related defects in epitaxially strained BTO films are absent and highly desirable.

V. CONCLUSION

Cube-on-cube-type epitaxial perovskite BTO films were grown on (001)STO substrates using different oxygen pressures. The crystal structure, ferroelectric properties, optical behavior, and electronic structure of the films were investigated. It was shown that the out-of-plane oriented dipolar $(V^{+2}{}_O\text{-}Ti^{3+})^+$ defects formed in the presence of in-plane compressive strain and oxygen deficiency. It was suggested that the in-plane compressive strain can reduce the formation energy for the out-of-plane oxygen vacancies, which leads to the out-of-plane orientation of the $(V^{+2}{}_O\text{-}Ti^{3+})^+$ dipoles.

ACKNOWLEDGMENTS

The authors acknowledge support from the European Structural and Investment Funds and the Ministry of Education, Youth, and Sports of the Czech Republic through Program "Research, Development, and Education" (Project No. SOLID21-CZ.02.1.01/0.0/0.0/16_019/0000760); the Czech Science Foundation (Grant No. 19-09671S); the Academy of Finland (Grant No. 298409); and the European Research Council (Advanced Grant No. 291132). The authors are grateful to M. Klinger, E. Heinonen, M. Savinov, and D. Chvostova for their assistance.

[1] M. E. Lines and A. M. Glass, *Principles and Applications of Ferroelectrics and Related Materials* (Clarendon Press, Oxford, 2004).

[2] *Physics of Ferroelectrics: A Modern Perspective*, edited by K. M. Rabe, C. H. Ahn, and J.-M. Triscone (Springer-Verlag, Berlin, 2007).

[3] K. Uchino, *Ferroelectric Devices* (Marcel Dekker, New York, 2000).

[4] J. F. Scott, *Ferroelectric Memories* (Springer-Verlag, Berlin, 2000).

[5] A. Janotti, J. B. Varley, M. Choi, and C. G. Van de Walle, Vacancies and small polarons in $SrTiO_3$, Phys. Rev. B **90**, 085202 (2014).

[6] V. E. Alexandrov, E. A. Kotomin, J. Maier, and R. A. Evarestov, First-principles study of bulk and surface oxygen vacancies in $SrTiO_3$ crystal, Eur. Phys. J. B **72**, 53 (2009).

[7] D. Gryaznov, E. Blokhin, A. Sorokine, E. A. Kotomin, R. A. Evarestov, A. Bussmann-Holder, and J. Maier, A comparative *ab initio* thermodynamic study of oxygen vacancies in ZnO and $SrTiO_3$: Emphasis on phonon contribution, J. Phys. Chem. C **117**, 13776 (2013).

[8] R. Evarestov, E. Blokhin, D. Gryaznov, E. A. Kotomin, R. Merkle, and J. Maier, Jahn-Teller effect in the phonon properties of defective $SrTiO_3$ from first principles, Phys. Rev. B **85**, 174303 (2012).

[9] E. Blokhin, E. Kotomin, A. Kuzmin, J. Purans, R. Evarestov, and J. Maier, Theoretical modeling of the complexes of iron impurities and oxygen vacancies in $SrTiO_3$, Appl. Phys. Lett. **102**, 112913 (2013).

[10] J. Kubacki, D. Kajewski, J. Goraus, K. Szot, A. Koehl, Ch. Lenser, R. Dittmann, and J. Szade, Impact of Fe doping on the electronic structure of $SrTiO_3$ thin films determined by resonant photoemission, J. Chem. Phys. **148**, 154702 (2018).

[11] *Ferroelectric Phenomena in Crystals*, edited by B. A. Strukov and A. P. Levanyuk (Springer, New York, 1998).

[12] S. Aggarwal and R. Ramesh, Point defect chemistry of metal oxide heterostructures, Annu. Rev. Mater. Sci. **28**, 463 (1998).

[13] A. Pramanick, A. Prewitt, J. Forrester, and J. L. Jones, Domains, domain walls and defects in perovskite ferroelectric oxides: A review of present understanding and recent contributions, Rev. Solid State Mater. Sci. **37**, 243 (2012).

[14] Y. S. Kim, D. J. Kim, T. H. Kim, T. W. Noh, J. S. Choi, B. H. Park, and J.-G. Yoon, Observation of room-temperature

ferroelectricity in tetragonal strontium titanate thin films on $SrTiO_3$ (001) substrates, Appl. Phys. Lett. **91**, 042908 (2007).

[15] M. Li, J. Zhou, X. Jing, M. Zeng, S. Wu, J. Gao, Z. Zhang, X. Gao, X. Lu, J.-M. Liu, and M. Alexe, Controlling resistance switching polarities of epitaxial $BaTiO_3$ films by mediation of ferroelectricity and oxygen vacancies, Adv. Electron. Mater. **1**, 1500069 (2015).

[16] Y. Heo, D. Kan, Y. Shimakawa, and J. Seidel, Resistive switching properties of epitaxial $BaTiO_{3-\delta}$ thin films tuned by after-growth oxygen cooling pressure, Phys. Chem. Chem. Phys. **18**, 197 (2016).

[17] A. Herklotz, D. Lee, E.-J. Guo, T. L. Meyer, J. R. Petrie, and H. N. Lee, Strain coupling of oxygen nonstoichiometry in perovskite thin films, J. Phys.: Condens. Matter **29**, 493001 (2017).

[18] U. Aschauer, R. Pfenninger, S. M. Selbach, T. Grande, and N. A. Spaldin, Strain-controlled oxygen vacancy formation and ordering in $CaMnO_3$, Phys. Rev. B **88**, 054111 (2013).

[19] U. Aschauer and N. A. Spaldin, Interplay between strain, defect charge state, and functionality in complex oxides, Appl. Phys. Lett. **109**, 031901 (2016).

[20] J. Xi, H. Xu, Y. Zhang, and W. J. Weber, Strain effects on oxygen vacancy energetics in $KTaO_3$, Phys. Chem. Chem. Phys. **19**, 6264 (2017).

[21] M. Klinger, L. Polivka, A. Jager, and M. Tyunina, Quantitative analysis of structural inhomogeneity in nanomaterials using transmission electron microscopy, J. Appl. Cryst. **49**, 762 (2016).

[22] V. Gartnerova, O. Pacherova, M. Klinger, M. Jelinek, A. Jager, and M. Tyunina, Strain fluctuations in $BaTiO_3/SrTiO_3$ heterostructures, Mat. Res. Bull. **89**, 180 (2017).

[23] E. Chernova, O. Pacherova, D. Chvostova, A. Dejneka, T. Kocourek, M. Jelinek, and M. Tyunina, Strain-controlled optical absorption in epitaxial ferroelectric $BaTiO_3$ films, Appl. Phys. Lett. **106**, 192903 (2015).

[24] A. Dejneka, D. Chvostova, O. Pacherova, T. Kocourek, M. Jelinek, and M. Tyunina, Optical effects induced by epitaxial tension in lead titanate, Appl. Phys. Lett. **112**, 031111 (2018).

[25] O. Pacherova, D. Chvostova, T. Kocourek, M. Jelinek, A. Dejneka, E. Eliseev, A. Morozovska, and M. Tyunina, Thermooptical evidence of carrier-stabilized ferroelectricity in ultrathin electrodeless films, Sci. Rep. **8**, 8497 (2018).

[26] See Supplemental Material at http://link.aps.org/supplemental/10.1103/PhysRevResearch.2.023056 for structural details.

[27] M. Tyunina, O. Pacherova, J. Peräntie, M. Savinov, M. Jelinek, H. Jantunen, and A. Dejneka, Perovskite ferroelectric tuned by thermal strain, Sci. Rep. **9**, 3677 (2019).

[28] *Landolt-Börnstein, Numerical Data and Functional Relationships in Science and Technology*, edited by K. H. Hellwege and A. M. Hellwege, New Series, Group III, Crystal and Solid State Physics (Springer, Berlin, 1981).

[29] O. Dieguez, S. Tinte, A. Antons, C. Bungaro, J. B. Neaton, K. M. Rabe, and D. Vanderbilt, *Ab initio* study of the phase diagram of epitaxial $BaTiO_3$, Phys. Rev. B **69**, 212101 (2004).

[30] V. B. Shirokov, Yu. I. Yuzyuk, B. Dkhil, and V. V. Lemanov, Phenomenological theory of phase transitions in epitaxial $BaTiO_3$ thin films, Phys. Rev. B **75**, 224116 (2007).

[31] T. Zhao, F. Chen, H. Lu, G. Yang, and Z. Chen, Thickness and oxygen pressure dependent structural characteristics of $BaTiO_3$ thin films grown by laser molecular beam epitaxy, J. Appl. Phys. **87**, 7442 (2000).

[32] S. B. Mia, C. L. Jia, T. Heeg, O. Trithaveesak, J. Schubert, and K. Urban, Heterostructures of $BaTiO_3$ bilayer films grown on $SrTiO_3$(001) under different oxygen pressures, J. Cryst. Growth **283**, 425 (2005).

[33] Y. L. Zhu, S. J. Zheng, D. Chen, and X. L. Ma, Microstructure tuning of epitaxial $BaTiO_{3-x}$ thin films grown using laser molecular beam epitaxy by varying the oxygen pressure, Thin Solid Films **518**, 3669 (2010).

[34] A. P. Chen, F. Khatkhatay, W. Zhang, C. Jacob, L. Jiao, and H. Wang, Strong oxygen pressure dependence of ferroelectricity in $BaTiO_3/SrRuO_3/SrTiO_3$ epitaxial heterostructures, J. Appl. Phys. **114**, 124101 (2013).

[35] J. Lyu, S. Estandía, J. Gazquez, M. F. Chisholm, I. Fina, N. Dix, J. Fontcuberta, and Fl. Sánchez, Control of polar orientation and lattice strain in epitaxial $BaTiO_3$ films on silicon, ACS Appl. Mater. Interfaces **10**, 25529 (2018).

[36] H. Arend and L. Kihlborg, Phase composition of reduced and reoxidized barium titanate, J. Am. Cer. Soc. **52**, 63 (1969).

[37] E. J. Granhed, A. Lindman, C. Eklof-Osterberg, M. Karlsson, S. F. Parker, and G. Wahnstrom, Band vs. polaron: Vibrational motion and chemical expansion of hydride ions as signatures for the electronic character in oxyhydride barium titanate, J. Mater. Chem. A **7**, 16211 (2019).

[38] J. E. Prieto and I. Markov, Stranski–Krastanov mechanism of growth and the effect of misfit sign on quantum dots nucleation, Surface Sci. **664**, 172 (2017).

[39] S. M. Yang, J. Y. Jo, T. H. Kim, J.-G. Yoon, T. K. Song, H. N. Lee, Z. Marton, S. Park, Y. Jo, and T. W. Noh, ac dynamics of ferroelectric domains from an investigation of the frequency dependence of hysteresis loops, Phys. Rev. B **82**, 174125 (2010).

[40] M. DiDomenico, Jr. and S. H. Wemple, Oxygen-octahedra ferroelectrics. I. Theory of electro-optical and nonlinear optical effects, J. Appl. Phys. **40**, 720 (1969).

[41] M. Zgonik, P. Bernasconi, M. Duelli, R. Schlesser, P. Gunter, M. H. Garrett, D. Rytz, Y. Zhu, and X. Wu, Dielectric, elastic, piezoelectric, electro-optic, and elasto-optic tensors of $BaTiO_3$ crystals, Phys. Rev. B **50**, 5941 (1994).

[42] J. R. Brews, Energy Band Changes in Perovskites Due to Lattice Polarization, Phys. Rev. Lett. **18**, 662 (1967).

[43] P. Geng, W. Li, X. Zhang, X. Zhang, Y. Deng, and H. Kou, A novel theoretical model for the temperature dependence of band gap energy in semiconductors, J. Phys. D: Appl. Phys. **50**, 40LT02 (2017), and references therein.

[44] R. F. Berger, C. J. Fennie, and J. B. Neaton, Band Gap and Edge Engineering via Ferroic Distortion and Anisotropic Strain: The Case of $SrTiO_3$, Phys. Rev. Lett. **107**, 146804 (2011).

[45] S. H. Wemple, Polarization fluctuations and the optical-absorption edge in $BaTiO_3$, Phys. Rev. B **2**, 2679 (1970).

[46] R. Scharfschwerdt, A. Mazur, O. F. Schirmer, H. Hesse, and S. Mendricks, Oxygen vacancies in $BaTiO_3$, Phys. Rev. B **54**, 15284 (1996).

[47] L. Samet, D. Imhoff, J.-L. Maurice, J.-P. Contour, A. Gloter, T. Manoubi, A. Fert, and C. Colliex, EELS study of interfaces in magnetoresistive LSMO/STO/LSMO tunnel junctions, Eur. Phys. J. B **34**, 179 (2003).

[48] M. Nord, P. E. Vullum, M. Moreau, J. E. Boschker, S. M. Selbach, R. Holmestad, and T. Tybell, Structural phases driven by oxygen vacancies at the $La_{0.7}Sr_{0.3}MnO_3/SrTiO_3$ hetero-interface, Appl. Phys. Lett. **106**, 041604 (2015).

[49] M. Bugnet, G. Radtke, S. Y. Woo, G. Zhu, and G. A. Botton, Temperature-dependent high energy-resolution EELS of ferroelectric and paraelectric $BaTiO_3$ phases, Phys. Rev. B **93**, 020102(R) (2016).

[50] M. Abbate, F. M. F. de Groot, J. C. Fuggle, A. Fujimori, Y. Tokura, Y. Fujishima, O. Strebel, M. Domke, G. Kaindl, J. van Elp, B. T. Thole, G. A. Sawatzky, M. Sacchi, and N. Tsuda, Soft-x-ray-absorption studies of the location of extra charges induced by substitution in controlled-valence materials, Phys. Rev. B **44**, 5419 (1991).

[51] C. Baeumer, C. Schmitz, A. Marchewka, D. N. Mueller, R. Valenta, J. Hackl, N. Raab, S. P. Rogers, M. I. Khan, S. Nemsak, M. Shim, S. Menzel, C. M. Schneider, R. Waser, and R. Dittmann, Quantifying redox-induced Schottky barrier variations in memristive devices via in operando spectromicroscopy with graphene electrodes, Nat. Commun. **7**, 12398 (2016).

[52] V. V. Laguta, A. M. Slipenyuk, I. P. Bykov, M. D. Glinchuk, M. Maglione, D. Michau, J. Rosa, and L. Jastrabik, Electron spin resonance investigation of oxygen-vacancy-related defects in $BaTiO_3$ thin films, Appl. Phys. Lett. **87**, 022903 (2005).

[53] E. Erdem, P. Jakes, R. A. Eichel, D. C. Sinclair, M. Pasha, and I. M. Reaney, Formation of $(Ti'_{Ti} - V_O^{\bullet\bullet})^{\bullet}$ defect dipoles in ($BaTiO_3$ ceramics heat-treated under reduced oxygen partial-pressure, Func. Mater. Lett. **3**, 65 (2010).

[54] L. Rusevich and E. Kotomin (unpublished).